Review

An Electrostatic Re-Evaluation of Catalysis across Diverse Ribonuclease Classes

Yongling Ying [1,2], Lan Zhang [1], and Fan Yang [1,*]

[1] School of Life Sciences and Technology, Harbin Institute of Technology, Harbin 150080, China
[2] Innovation Photonics and Imaging Center, School of Instrumentation Science and Engineering, Harbin Institute of Technology, Harbin 150080, China
* Correspondence: fanyang115@hit.edu.cn

Received: 8 May 2026; Revised: 16 June 2026; Accepted: 20 July 2026; Published: 3 November 2026

Abstract: The catalytic efficiency of ribonucleases (RNases) is conventionally attributed to specific acid-base residues, metal cofactors, and conformational dynamics. Their apparent structural diversity may nevertheless reflect shared electrostatic principles that contribute to catalysis. In this review, we examine diverse RNase classes, including metal-independent, metal-dependent, and atypical toxin families, through the classic concept of electrostatic catalysis. Based on recent kinetic and thermodynamic data, such as heavy-atom kinetic isotope effects, substantial pK_a shifts, and computational free energy profiles, we argue that RNase active sites can be understood as preorganized electrostatic environments that substantially contribute to catalysis. The protein scaffold rigidly positions a localized electric field to neutralize the accumulating negative charge of the pentacovalent phosphorane transition-state structure of the RNA substrate. Importantly, to avoid thermodynamic traps, natural RNases spatially segregate initial RNA recruitment from chemical catalysis. Extended cationic surfaces or accessory domains recruit the substrate by releasing its condensed counterions, driving an entropically favorable association. Decoupling long-range binding from transition-state stabilization allows these enzymes to optimize both affinity and turnover. These mechanisms may provide a conceptual framework for the rational design of artificial ribonucleases and compact, programmable biocatalysts for targeted RNA degradation.

Keywords: ribonuclease; electrostatic preorganization; targeted RNA degradation

1. Introduction

Cellular RNA levels depend on a strict balance between transcription and degradation. Ribonucleases (RNases) control the latter half of this equation. They operate across diverse biological pathways, ranging from processing RNA precursors to monitoring transcript quality [1–6]. By accelerating the hydrolysis of chemically stable phosphodiester bonds by up to 10^{15}-fold, RNases guarantee that dynamic RNA turnover and gene regulation proceed on biologically relevant timescales [7]. As outlined in Figure 1, they regulate gene expression, sense pathogenic RNA during innate immune responses [8–15], and have been exploited to develop precise tools for nucleic acid detection, molecular diagnosis, and targeted therapeutics [16,17]. For example, a promising RNA regulation strategy, ribonuclease-targeting chimeras (RIBOTACs), could recruit endogenous RNases L to eliminate specific disease-related microRNAs [18,19].

Given their important roles in cellular RNA metabolism and promising applications in therapeutic intervention, for more than half a century, scientists have devoted considerable effort to answering one central question: What are the molecular mechanisms underlying each class of RNases? A common way to classify RNase mechanisms is based on their cofactor requirements, generally divided into metal-independent (acid-base) and metal-dependent enzymes. The metal-independent class, represented by the RNase A and RNase T1 families, typically relies on precisely arranged histidine or glutamate, to execute general acid-base catalysis [20–22]. In the 2′-O-transphosphorylation reaction, these RNases use a general base to activate the 2′-hydroxyl nucleophile and a general acid to protonate the 5′-leaving group, yielding a 2′,3′-cyclic phosphate intermediate and a 5′-hydroxyl product. The metal-dependent class, including RNase H and RNase III, commonly uses Mg^{2+} ions in the active site [23–25], coordinated by conserved acidic residues (e.g., the DEDD motif), to activate the nucleophile (often a water molecule) to drive RNA hydrolysis [26–28].

Copyright: © 2026 by the authors. This is an open access article under the terms and conditions of the Creative Commons Attribution (CC BY) license (https://creativecommons.org/licenses/by/4.0/).
Publisher's Note: Scilight stays neutral with regard to jurisdictional claims in published maps and institutional affiliations

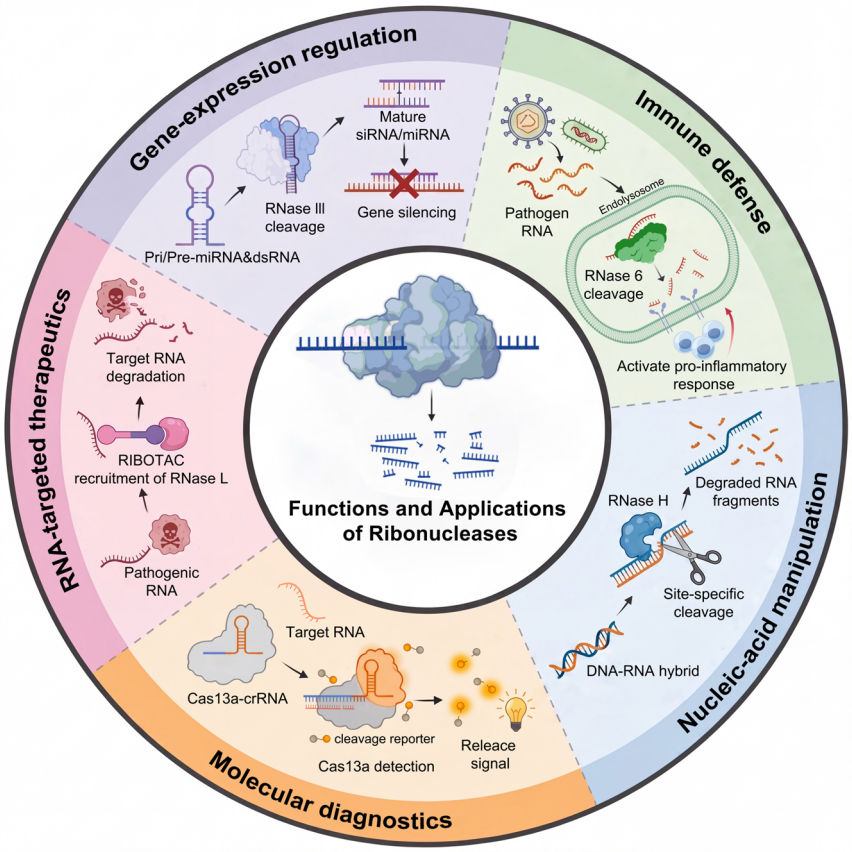


Figure 1. Endogenous functions and biotechnological applications of ribonucleases. Regulation of gene expression: RNase III family enzymes (Drosha/Dicer) execute the sequential processing of precursor RNA transcripts into mature miRNAs for mRNA translational repression. Immune defense: RNase 6 cleaves internalized pathogenic RNAs to generate uridine-terminated breakdown products, which serve as essential ligands for TLR8 activation and the subsequent pro-inflammatory cascade. Nucleic acid manipulation: RNase H specifically degrades the RNA moiety within RNA:DNA hybrids, a property essential for reverse transcription and genome engineering. Molecular diagnostics: Programmable Cas13 effectors couple crRNA-guided target recognition to collateral RNA trans-cleavage, yielding an amplifiable fluorescent readout. RNA-targeted therapeutics: RIBOTACs act as proximity-inducing chimeras that harness endogenous RNase L to selectively cleave targeted pathogenic RNAs.

While scientists have focused on the cofactor dependence and apparent structural fold diversity of RNases, modern biophysical and computational studies increasingly point to electrostatic preorganization as a fundamental physical mechanism of all enzymes [29–31]. Therefore, in this review, we re-evaluate ribonucleases, selectively integrating structural, kinetic, thermodynamic and computational studies to re-examine RNase catalysis from the perspective of electrostatic preorganization. Whether employing an oriented network of charged residues or recruiting divalent metal cations, RNases use their structural scaffolds to generate precise, oriented electric fields within their active sites [32]. These preorganized fields selectively stabilize the transition-state charge distribution relative to the ground state, thereby reducing the energetic penalty associated with solvent reorganization [33,34]. By elucidating the shared physical principles governing diverse RNases, we aim to better understand their functional evolution and guide the rational design of RNA-processing biocatalysts.

2. Structural Scaffold for Electrostatic Preorganization and Transition-State Stabilization

The transphosphorylation or hydrolysis of RNA proceeds via an associative pathway, forming a high-energy pentacovalent phosphorane transition-state structure [35]. Negative charge accumulates on the non-bridging phosphoryl oxygens. Catalytic efficiency requires lowering the activation free energy barrier by stabilizing this specific charge distribution more effectively than the ground state [33,36]. As shown in Figure 2a, in solution, water molecules must reorient their dipoles dynamically to accommodate the developing charge, paying a substantial thermodynamic cost. By contrast, ribonucleases utilize their three-dimensional structures to generate a preorganized electrostatic landscape to overcome this penalty [29]. The protein scaffold pre-positions polar groups

within the active site into a catalytically optimal geometry, to exert an oriented electric field [30,34], with the entropic cost compensated by the overall folding free energy. RNases thus provide a "pre-paid" electrostatic environment that minimizes reorganization energy. This principle of structural preorganization is observed across major classes of ribonucleases.

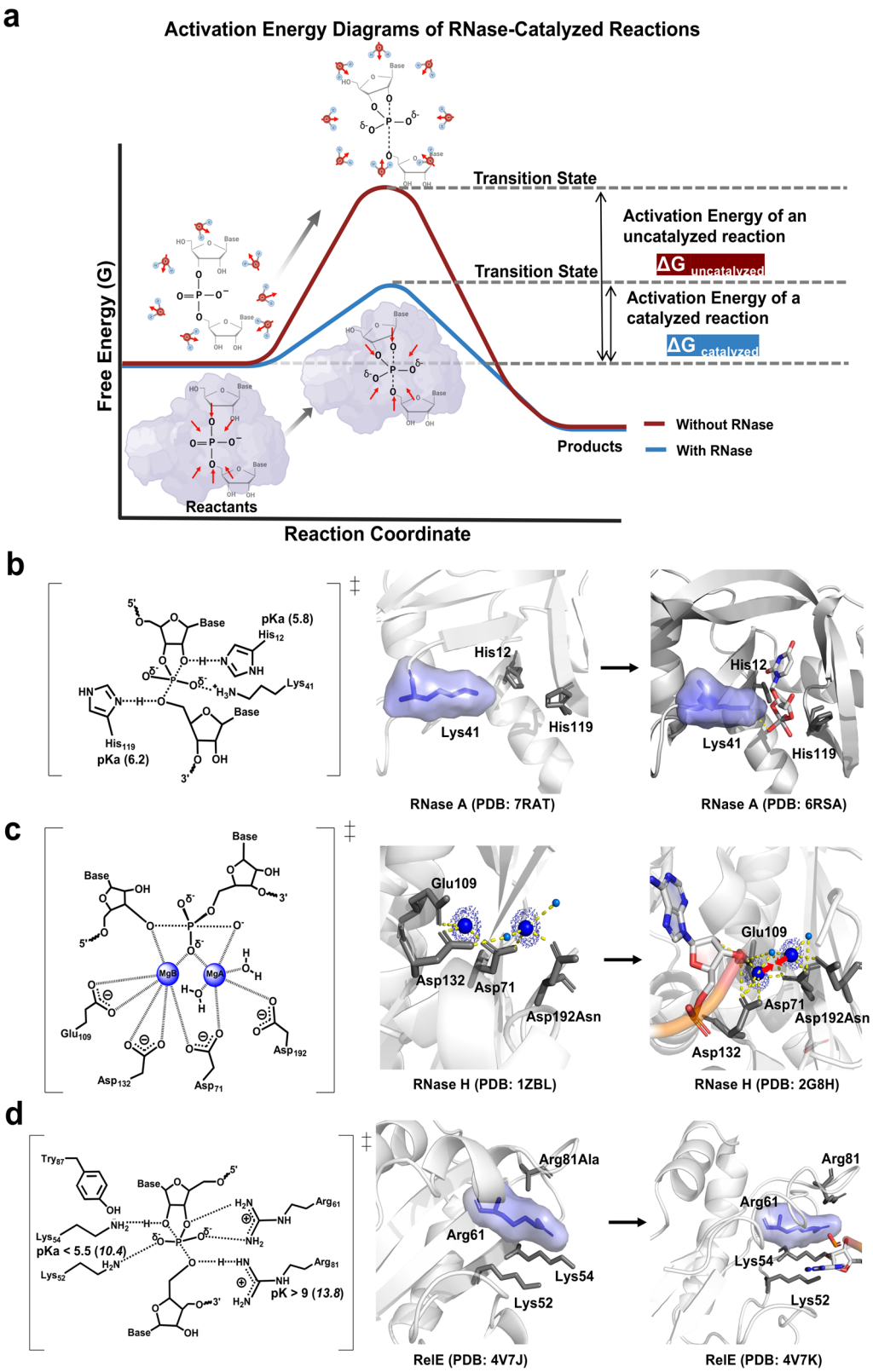


Figure 2. Electrostatic preorganization and transition-state stabilization across diverse ribonucleases. (**a**) Thermodynamic and electrostatic basis of RNA cleavage. The free energy profiles compare the RNase-catalyzed (blue line) and uncatalyzed (red line) pathways, showing the reduced $\Delta G^{\ddagger}$ between the reactant state (RS) and the

transition state (TS). Unlike bulk water, the preorganized active site provides complementary electrostatic stabilization to the pentacovalent phosphorus, minimizing the environmental reorganization penalty. (**b**–**d**) Mechanistic and electrostatic models for representative RNases. Each panel details the chemical mechanism (**left**), alongside the spatial orientation and local electrostatic potential of key residues in both RS (**middle**) and the TS (**right**). Structural figures were prepared using the PyMOL Molecular Graphics Systems, version 3.0.3 Schrodinger, LLC. (**b**) RNase A. The protein scaffold preorganizes the Lys41 side chain to form a hydrogen bond with the transition-state structure. (**c**) RNase H. A dynamic two-metal-ion motif drives catalysis. The metal ions undergo a cooperative contraction to neutralize the TS. (**d**) RelE toxin. Basic side chains mediate catalysis. Arg61 and Lys52 are pre-positioned to stabilize the transient geometry of the TS.

2.1. Electrostatics in the Context of Acid-Base Catalysis: The RNase A and T1 Families

In classical metal-independent ribonucleases, the structural scaffold directly preorganizes a group of amino acid side chains to project a localized cationic electric field. In the case of RNase A, the active site cleft precisely positions the catalytic triad (His12, His119, and Lys41 in PDB: 7RAT) [20,37]. While His12 and His119 function as the classical acid-base pair, Lys41 plays an indispensable role in transition-state stabilization. During the catalytic step, Lys41 points its positively charged ε-amino group directly toward the scissile phosphate, thereby helping neutralize the accumulating negative charge [38–40] (Figure 2b). Both kinetic and structural data explicitly uncouple its role of exerting preorganized electric field from ground-state substrate binding. Previous kinetic studies indicate that, mutation of Lys41 to alanine reduces catalytic efficiency k_{cat}/K_M by 10^4-fold, while the change in the Michaelis constant (K_M) is only 10-fold [7,41,42]. This demonstrates that the side chain geometry of Lys41 is designed to maximize electrostatic interactions with the pentacovalent transition-state structure, instead of being a primary ground-state anchor. A structurally analogous strategy is also observed in the RNase T1 family, where its active-site structure ensures the guanidinium group of Arg77 remains rigidly oriented toward the scissile phosphate [22,43]. In these RNases, to drive RNA cleavage, protein acts as a structural scaffold to selectively lower the activation barrier, demonstrating how preorganized electrostatics operate synergistically with general acid-base catalysis. Despite the key role of electrostatics in RNase A and T1 families, we still need to emphasize that, electrostatic preorganization does not replace the classical acid-base mechanism, rather, it provides the essential energetic environment that tunes their effectiveness.

2.2. The Metal Ion Scaffold: The RNase H and RNase III Families

Instead of relying on basic amino acid side chains, metal-dependent ribonucleases, such as RNase H and RNase III families, use divalent metal cations, typically Mg^{2+}, for electrostatic transition-state stabilization [23,25,44]. This class of RNases features a rigid anionic scaffold within their active site, such as the canonical DEDD motif in RNase H and the signature acidic cluster in RNase III [27]. They preorganize these acidic side chains into a specific coordination geometry that recruits two metal ions, Metal A and B, to generate a stronger electrostatic potential [45–48]. The electric field generated by this confined metal cluster is uncoupled from ground-state substrate binding, just like the role of Lys41 in RNase A. Previous kinetic studies reveal that, in *E. coli* RNase III, substituting the conserved Asp45 with alanine abolishes metal coordination and reduces its catalytic efficiency by approximately 30,000-fold. Yet, the capability of ground-state binding remains comparable to the wild-type enzyme ($K_D \sim 4.5$ nM versus 3.9 nM) [49]. This confirms that, in structural scaffolds of metal-dependent RNases, the metal-induced electric field is generated to stabilize the transition-state structure, rather than to anchor the RNA substrate. Structural and computational studies further reveal how this structural design operates during catalysis. In RNase H, the protein structure directs a cooperative contraction, moving the two Mg^{2+} ions from a resting separation of ~4.2 Å to ~3.8 Å in the transition-state structure [28,45,50–52] (Figure 2c), effectively neutralizing the accumulating negative charge on it. To better stabilize transition-state structure, Ribonucleases such as RNase H1 can also recruit a transient third metal ion to specific sites, employing cation trafficking dynamically to rebuild the active-site electric field [23,53,54].

2.3. Atypical Ribonucleases: The RelE Toxin Family

In contrast to classical metal-dependent and -independent RNase classes, an atypical RNase, RelE toxin family achieves electrostatic preorganization through an apparently different mechanism. Lacking obvious candidates for general acid-base catalysis or metal-binding acidic cluster [55], the RelE structural scaffold positions a cluster of basic residues (e.g., Arg61, Arg81, Lys52, Lys54 in PDB: 4V7K) around the scissile phosphate [56] (Figure 2d). Although RelE lacks the canonical acid-base pair found in RNase A-like enzymes, recent biochemical studies demonstrate that, in RelE structure, Arg81 and Lys54 experience a dramatic pK_a shift

of ~4.8 and ~4.9, respectively, supporting a potential acid-base catalysis with Lys54 (pK_a < 5.5) as the general base and Arg81 (pK_a > 9) as the general acid. Similar to RNase A, another key residue within this preorganized cationic cluster, Arg61, functions primarily to stabilize the transition-state structure, rather than to anchor the ground-state RNA substrate. Under single-turnover conditions, substituting Arg61 with alanine reduces k_{cat} by 2.7 × 10^6-fold, yet the ground-state binding affinity remains comparable to the wild type (K_D ~ 0.9 μM versus 3.2 μM). In addition, K52A shows a significant decrease of k_{cat} by 2.1 × 10^3-fold with only 6-fold change of K_D. By compressing basic amino acids into a highly localized region, RelE constructs a "pre-paid" electrostatic environment compensated by its overall folding energy. The resulting local electric field perturbs the chemical environment drastically to make substantial local pK_a shifts. Overall, RelE is an atypical RNase, which uses an electrostatic transition-state stabilization mechanism that facilitated by general acid-base catalysis [57].

3. Kinetic and Thermodynamic Evidence of Electrostatics

Validating structural models of electrostatic preorganization described above, it normally requires direct measurement of the transition-state charge distribution and the local electric fields. Recent advances in vibrational Stark effect (VSE) spectroscopy have provided direct experimental evidence of this concept. For example, VSE measurements on ketosteroid isomerase (KSI) demonstrate that, to drive catalysis, preorganized active-site structure of an enzyme can project local electric fields as large as ~144 MV/cm [30]. For ribonucleases, direct VSE probing of the scissile phosphate remains chemically challenging. However, recent advances in heavy-atom kinetic isotope effects (KIEs), phosphorothioate substitutions, and quantitative pH-rate analyses provide thermodynamic and kinetic parameters to test the electrostatic hypothesis [34,38,58]. They directly measure how the protein microenvironment alters local electrostatics, such as shifting the pK_a of catalytic residues or reducing the activation free energy barrier ($\Delta G^{\ddagger}$), supporting that electrostatic catalysis appears to be a major physical contributor to RNA cleavage across several well-characterized ribonuclease families.

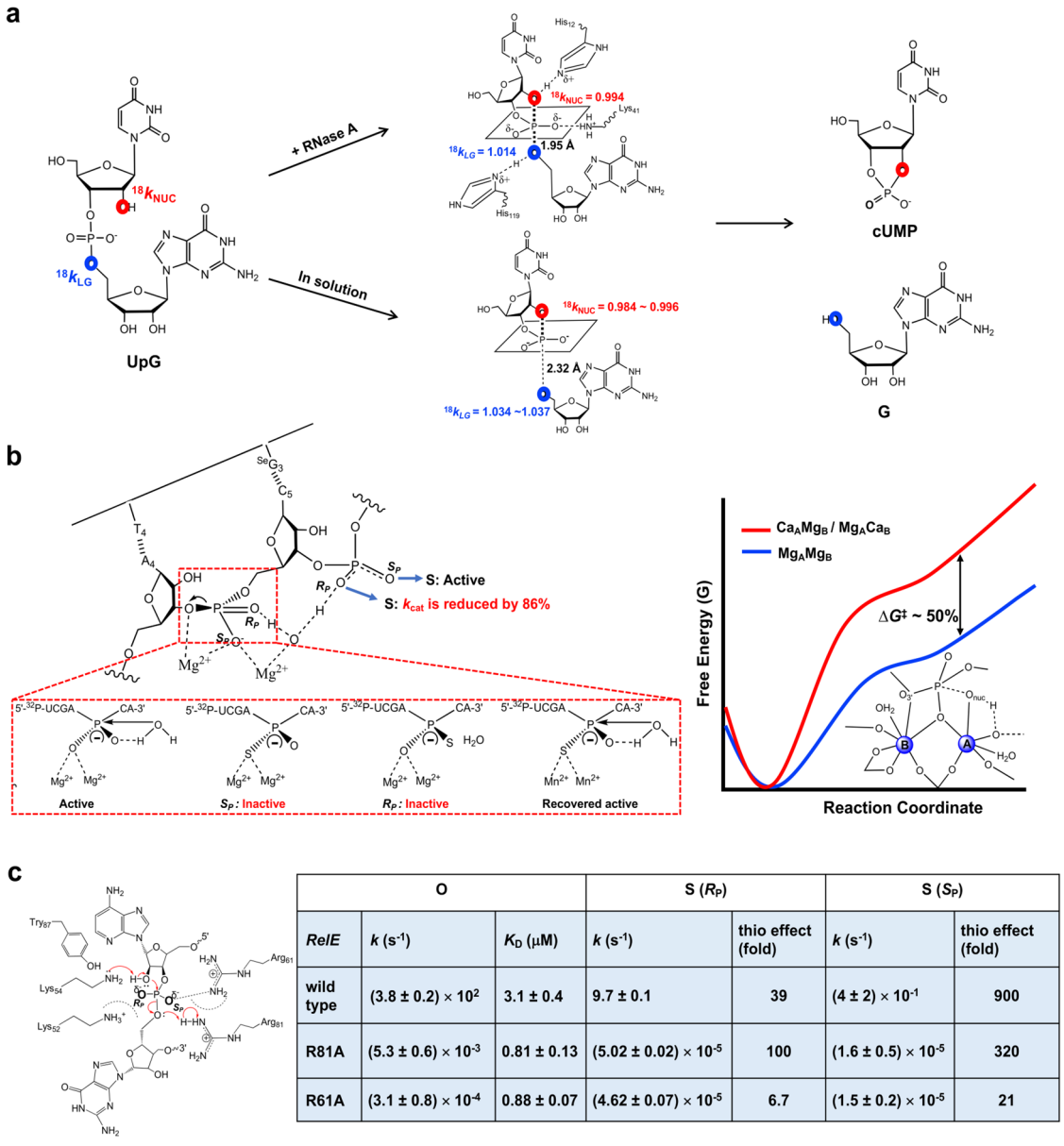
3.1. Metal-Independent Ribonucleases

For metal-independent ribonucleases, kinetic isotope effects provide the most direct information of the transition-state charge distribution. Recently, heavy-atom ^{18}O KIEs on RNase A-catalyzed RNA cleavage indicate a late, associative transition-state structure, strongly supporting electrostatic preorganization effect from the enzyme [38]. KIEs are typically measured through competitive methods using a mixture of ^{16}O- and ^{18}O- labeled substrates, with the isotope effect expressed as the ratio of rate constants for the light and heavy isotopologues ($^{18}k = k_{16}/k_{18}$). As depicted in Figure 3a, a looser transition-state bonding environment preferentially accelerates the light isotopologue, thus yielding a greater ^{18}k. In the nonenzymatic solution 2′-*O*-transphosphorylation reaction of uridylyl-3′-guanosine (UpG), the leaving group KIE ($^{18}k_{LG}$) is large (1.034–1.037), suggesting that the 5′ O-P bond must be almost completely broken to reach the transition state. In contrast, in a RNase A-catalyzed reaction, the protein microenvironment significantly reduces $^{18}k_{LG}$ (1.014) while simultaneously maintaining an inverse nucleophile KIE ($^{18}k_{NUC}$ < 1), indicating a more compact transition-state structure featuring advanced 2′ O-P bond formation and less advanced 5′ O-P bond cleavage. This compact geometry results in substantial negative charge accumulation onto the non-bridging phosphoryl oxygens, which is energetically unfavorable in bulk water. Molecular dynamics (MD) and quantum mechanical (QM) simulations also show that, preorganized electrostatic network within the RNase A active site stabilizes the negative charge of the transition-state structure effectively [38]. This cationic cleft also perturbs the microscopic pK_a values of His12 and His119 to ~5.8 and ~6.2, respectively, optimizing their proton affinities for concerted general acid-base catalysis at physiological pH.

3.2. Metal-Dependent Ribonucleases

In metal-dependent RNases, the thermodynamic contribution of the preorganized electric field can be assessed through atomic substitution at the scissile phosphate and the corresponding change of free energy profiles. Sulfur substitution of oxygen disrupts Mg^{2+} coordination and weakens its hydrogen bond with water molecule, which causes a significant defect on localized electrostatic stabilization. Accordingly, in RNA cleavage reaction catalyzed by metal-dependent RNase, phosphorothioate modification makes a highly precise probe to map the electrostatic locus of the metal-ion catalyst at atomic resolution. For *E. coli* RNase H1, replacing the scissile phosphate oxygen with sulfur strictly abolishes catalytic RNA cleavage, an effect that can be chemically rescued by thiophilic metal ions like Mn^{2+} (Figure 3b). Moreover, replacing the pro-R_P non-bridging oxygen immediately 3′ to the scissile bond with sulfur reduces the catalytic turnover (k_{cat}) by 86%, whereas pro-S_P substitution has no such effect. This profound stereospecific activity difference demonstrates a strict kinetic requirement for a precise hydrogen-bonding network, at the correct position, to neutralize the developing negative charge [23,59]. Metal

substitution is another way of addressing the electrostatic function of metal-dependent RNases. As described in the section 2.2, in a RNase H-catalyzed reaction, to neutralize the pentacovalent transition-state structure, two Mg^{2+} ions experience a cooperative contraction. In addition, QM/MM studies show that the catalytic efficiency relies on the precise charge density and ionic radius of Mg^{2+} (~0.7 Å) [46]. Substituting single Mg^{2+} with a larger, but less polarizing Ca^{2+} (~1.0 Å) increases the free energy barrier $\Delta G^{\ddagger}$ by ~50% (from ~17 kcal/mol to ~25 kcal/mol for CaMg, ~24 kcal/mol for MgCa). The metal substitution abolishes RNA cleavage, but still maintains a nearly identical ground-state binding geometry, confirming that the two-metal motif functions as a highly geometrically restrictive and precisely tuned electrostatic environment for transition-state stabilization.



c

	O		S (R_P)		S (S_P)	
RelE	*k* (s^{-1})	K_D (μM)	*k* (s^{-1})	thio effect (fold)	*k* (s^{-1})	thio effect (fold)
wild type	$(3.8 \pm 0.2) \times 10^{2}$	3.1 ± 0.4	9.7 ± 0.1	39	$(4 \pm 2) \times 10^{-1}$	900
R81A	$(5.3 \pm 0.6) \times 10^{-3}$	0.81 ± 0.13	$(5.02 \pm 0.02) \times 10^{-5}$	100	$(1.6 \pm 0.5) \times 10^{-5}$	320
R61A	$(3.1 \pm 0.8) \times 10^{-4}$	0.88 ± 0.07	$(4.62 \pm 0.07) \times 10^{-5}$	6.7	$(1.5 \pm 0.2) \times 10^{-5}$	21

Figure 3. Kinetic, thermodynamic, and computational evidence for electrostatic transition-state stabilization across diverse RNases. (**a**) Metal-independent RNases. KIEs indicate a compact, late associative transition-state structure featuring advanced 2′ O-P bond formation and less advanced 5′ O-P bond cleavage, which is effectively stabilized by the preorganized electrostatic network within the active site of RNase A (Left and right panels were adapted with permission for noncommercial use from Gu et al. [38]. Copyright 2013 by the authors. Transition-state structures in the middle were adapted with permission from Raines [42]. Copyright 1998 American Chemical Society). (**b**) Metal-dependent RNases. Probing the electrostatic contribution of the two-metal-ion scaffold in RNase H. Phosphorothioate modification of specific non-bridging oxygens at and immediately 3′ to the scissile phosphate disrupts the local electrostatic network, thereby severely affecting catalytic activity (left panel, adapted with permission from Abdur et al. [60]. Copyright 2014 International Union of Crystallography). Computed free energy profiles reveal that substituting the polarizing Mg^{2+} with Ca^{2+} increases the activation barrier by 50% (right

panel, adapted from Rosta et al. [46] under the terms of the ACS AuthorChoice License). (**c**) Atypical RNases. Kinetic data using sulfur-substituted mRNA substrates identify specific residues, such as Arg61, as primary contributors to neutralizing the developing negative charge (Adapted with permission from Dunican et al. [57]. Copyright 2015 American Chemical Society).

3.3. Atypical Ribonucleases: The RelE Toxin Family

RelE toxin lacks a canonical acid-base catalytic pair. Instead, abundant kinetic analyses support that its cationic active site accelerates RNA cleavage primarily through electrostatic transition-state stabilization [57]. Single-turnover kinetics show that substituting Arg61 or Arg81 with alanine reduces the cleavage rate by 2.7×10^6-fold and 6.0×10^4-fold, respectively, without altering the ground-state binding affinity ($K_D \sim 0.8$–3.0 μM) [55]. Same as in the metal-dependent RNases, phosphorothioate substitution at scissile phosphate helps isolate the thermodynamic contribution of specific electrostatic contacts from RelE. In this case, substituting the non-bridging oxygen with a soft sulfur atom disrupts the pre-existing electrostatic network, the localized electric fields projected by cationic residues, thus mapping the exact spatial origin of electrostatic field at atomic resolution. Wild-type RelE exhibits a 900-fold thio-effect for the S_P stereoisomer, compared to the 39-fold effect for the R_p stereoisomer, suggesting its strong electrostatic dependence on the pro-S_P non-bridging oxygen (Figure 3c). Interestingly, mutating Arg61 to alanine attenuates this S_P thio-effect to 21-fold, serving a strong kinetic evidence that Arg61 side chain is the origin of the electric field stabilizing the transition-state structure [57]. Moreover, kinetic pH-rate profiling reveals the substantial thermodynamic consequences of this dense cationic microenvironment [58]. As described in section 2.3, the local electric field perturbs the pK_a of the general acid and base, Arg81 and Lys54, by ~5 units from its unperturbed values. Through 5′-phosphorothiolate substitution of the bridging oxygen, the rate defect of the R81A mutant is efficiently rescued, confirming its specific role as the general acid in the chemical step.

4. Electrostatics in Substrate Recognition and Binding

In Sections 2 and 3, we described how ribonucleases accelerate the RNA cleavage through electrostatic preorganization and transition-state stabilization. Although preorganized active-site electric field lowers the chemical activation barrier, initial recruitment of polyanionic RNA from bulk solution is indeed another thermodynamic challenge. Taking advantage of electrostatics again, RNases overcome this by projecting long-range positive electrostatic potentials for electrostatic steering, driving substrate association beyond the diffusion limit. To avert a thermodynamic trap that would otherwise increase the activation free energy, the ground-state binding affinity of the RNA substrate is precisely tuned. This necessitates spatial segregation of electrostatic functions for RNases: highly localized fields stabilize the pentacovalent transition-state structure, while distinct cationic surfaces or specialized accessory modules mediate initial ground-state recruitment.

4.1. Extended Electrostatic Steering and Polyelectrolyte Interactions

In the RNase A superfamily, substrate recruitment relies on an extended cationic cleft that is structurally distinct from the primary catalytic center [39]. In solution, the highly charged RNA polyanion is shielded by a dense atmosphere of counterions. Upon binding, the extended cationic surface of the RNase displaces this ionic cloud, releasing the counterions into bulk water to provide a massive entropic driving force for complex formation. This extended electrostatic effect is markedly amplified in divergent human RNase A homologs evolved for innate immunity, such as RNase 3 (ECP) and RNase 7 [61–65]. As shown in Figure 4a,b, human RNase 3 and RNase 7 use an auxiliary Arg/Lys-rich cationic surface to mediate substrate binding, distinct from the catalytic center. Unlike RNase 3, which possesses an arginine-rich motif, RNase 7 uses a cluster of lysine side chains (an extreme +16 net charge) to generate a broad cationic surface that rapidly recruits and binds RNA polyanions. This evolutionary adaptation demonstrates that long-range Coulombic forces provide a major driving force for substrate recruitment, functioning as a ground-state anchor rather than a direct chemical activator.

4.2. Electrostatic Readout of RNA Geometry: The RNase III Superfamily

When processing highly structured RNA substrates like double-stranded RNA (dsRNA), RNases use accessory domains to “read out” specific charge topologies. The RNase III superfamily, including the eukaryotic microRNA processing enzymes Dicer and Drosha, employs double-stranded RNA-binding domains (dsRBDs) to detect the spatial distribution of 2′-hydroxyl dipoles and phosphate charges unique to A-form helices [24,66–69] (Figure 4c). As observed in yeast RNase III (Rnt1p), the RNase employs a double-ruler mechanism to ensure the precision of cleavage. The dsRBD1 and N-terminal domain dimer, working synergistically, measure the exact

distance (16 and 14 base pairs) from a terminal AGNN tetraloop down to the scissile phosphate (Figure 4d). Because this interaction relies on 3D structure and electrostatics rather than base-pairing sequence complementarity, the recruitment module functions as a stringent electrostatic filter: only substrates with the correct charge landscape are physically loaded into the catalytic valley for metal-ion-mediated cleavage.

4.3. Terminal Charge Sensing and RNP Assembly: Exoribonuclease Xrn1 and RNase P

To regulate RNA decay, an alternative electrostatic recruitment strategy involves the selective sensing of RNA terminal phosphorylation states. Much like the bacterial endoribonuclease RNase E and the bifunctional RNase J, the 5′-3′ mRNA exoribonuclease Xrn1 employs a spatially segregated, highly basic pocket to specifically recognize 5′-monophosphorylated mRNA substrates [47,70,71] (Figure 4e). Crystal structural data shows that this 5′-monophosphate is anchored by a conserved cluster of basic residues (e.g., Lys93, Arg100, Arg101 in PDB: 2Y35), which is physically uncoupled from the catalytic center. This specific 5′-monophosphate recognition selectively excludes RNAs with the 5′-triphosphate, thereby ensuring the fidelity of mRNA turnover [72,73]. In ribonucleoprotein (RNP) complexes such as bacterial RNase P, extended electrostatic recruitment is mediated by a protein cofactor (Figure 4f). While the catalytic RNA (P RNA) uses metal ions for catalytic reaction, the associated basic RnpA protein subunit directly contacts the pre-tRNA 5′-leader [3,74–76]. This protein-mediated electrostatic anchoring drives ground-state association, neutralizes the Coulombic repulsion between the polyanionic substrate and the ribozyme core, operating independently of the precise metal-dependent transition-state stabilization within the RNA active site.

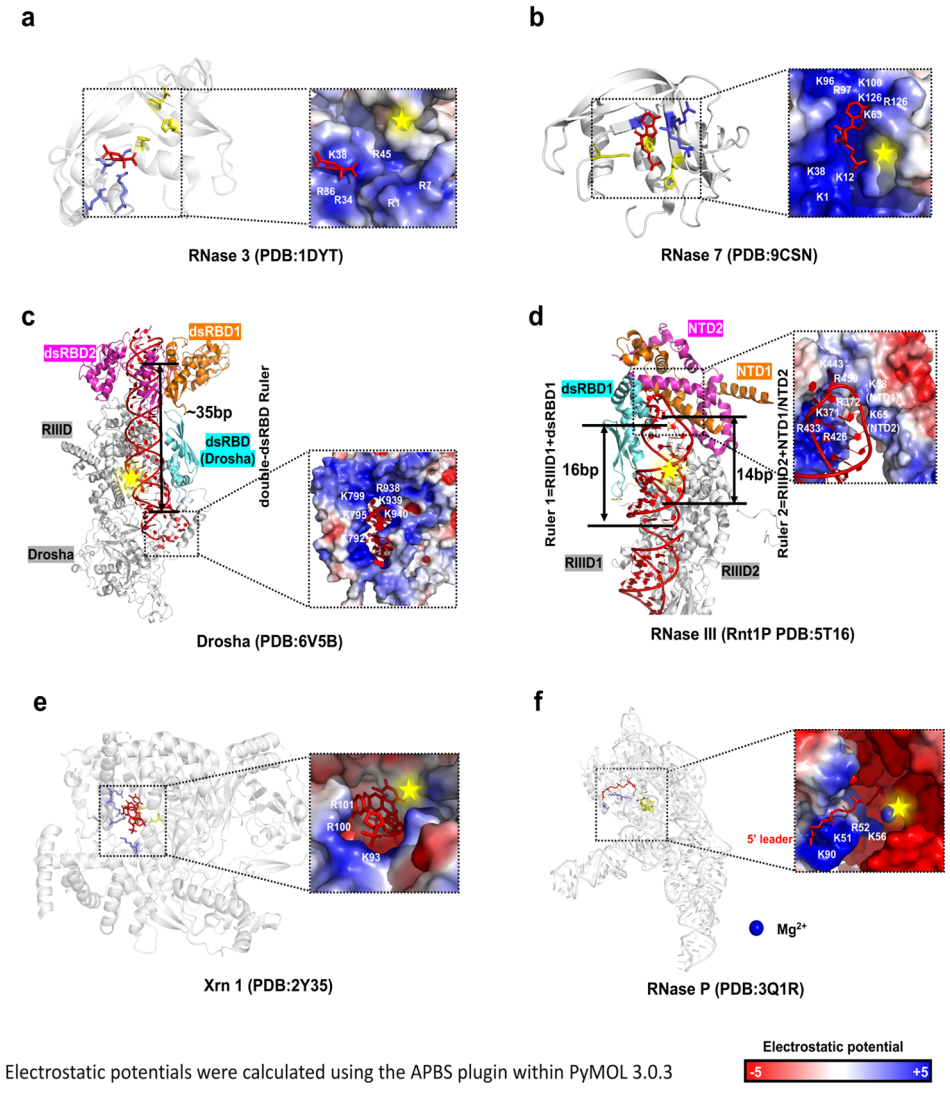


Figure 4. Spatial segregation of electrostatic substrate recruitment and chemical catalysis. Global structures of representative ribonucleases and close-up views of distal electrostatic modules mediating ground-state RNA capture. A consistent color-coding scheme is used for all structural representations: RNA in red and the catalytic center as a yellow star. For electrostatic potential surfaces, positively and negatively charged regions are colored

blue and red, respectively (scale bar at the bottom right). (**a**) RNase 3 and (**b**) RNase 7. Broad cationic surfaces drive long-range electrostatic steering to anchor the substrate. (**c**) Drosha and (**d**) RNase III. Accessory domains and dsRBDs serve as electrostatic "rulers", dictating precise cleavage registers by probing dsRNA charge topologies. (**e**) Xrn1. A spatially distinct basic pocket specifically locks onto the 5′-monophosphoate of mRNA substrates. (**f**) RNase P. The cationic RnpA protein subunit anchors the pre-tRNA 5′-leader for distal charge screening, structurally decoupled from the transition-state stabilization within the ribozyme core.

5. Conclusions and Perspectives

When surveyed across different RNase families, a unifying theme is that the catalytic proficiency of diverse ribonucleases fundamentally emerges from precisely tuned electrostatic environments. Rather than relying exclusively on the active site for target recognition, these enzymes use distal auxiliary surfaces or domains to exploit entropically favored counterion release, thereby driving robust ground-state substrate recruitment. Once the RNA is securely anchored, the preorganized catalytic core takes over to project a focused, intense electric field. Whether this local field is mediated by the acid-basic residue networks in RNase A and RelE, or by the precisely coordinated metal ions in RNase III and RNase H, it functions in concert with catalytic residues or metal ions to orchestrate nucleophile activation, neutralize the high-energy pentacovalent transition state, and facilitate leaving group departure. Ultimately, by topologically decoupling initial substrate binding from pK_a perturbation and transition-state stabilization, RNases elegantly avoid the thermodynamic traps associated with ground-state over-stabilization, thereby achieving rapid and efficient catalytic turnover.

Translating our mechanistic understanding of natural ribonucleases into the rational design of artificial ribonucleases (aRNases) remains a formidable yet compelling challenge. As the field of RNA-targeted therapeutics expands, these engineered biocatalysts could offer a valuable complementary strategy to bacterial CRISPR-Cas systems, potentially mitigating concerns regarding their immunogenicity and collateral cleavage [16,77–81]. Inspired by the spatial segregation observed in nature, aRNases might be conceptually constructed through the asymmetric dimerization of canonical RNA-binding domains, like RNA recognition motifs (RRMs) or K homology (KH) domains. In this proposed architecture, one subunit functions as a sequence- or structure-specific ground-state anchor, allowing the other to project a localized catalytic electric field toward the scissile phosphate. By design, this division of labor aims to decouple substrate recruitment from chemical catalysis, preventing the enzyme from falling into the thermodynamic traps associated with ground-state over-stabilization. Nevertheless, generating a catalytically competent active site requires far more than the mere accumulation of basic amino acids within a synthetic pocket. Attaining biologically relevant enzymatic proficiency will likely depend on the precision of modern computational enzymology, including QM/MM and molecular dynamics, to rigidly pre-organize arginine, lysine, or histidine clusters. This tailored local field is required to sufficiently complement the transition-state geometry to introduce the requisite pK_a shifts and neutralize the accumulating negative charge during 5′ O-P bond scission. From a translational perspective, the compact nature of these artificial scaffolds may also offer distinct advantages for cellular delivery. Small, artificial scaffolds containing cationic patches may facilitate cellular association or uptake, although nonspecific binding, cytotoxicity, and delivery efficiency would require careful optimization [82,83]. By enriching these miniaturized proteins with extended cationic patches, aRNases might simultaneously exploit long-range electrostatic steering to locate target transcripts in the crowded cytosol and lower the kinetic barrier for potentially enhanced cellular entry. Ultimately, the evolution from describing natural ribonucleases to engineering programmable RNA-degrading biocatalysts represents a logical progression for the field, one that holds considerable but still preliminary promise for advancing synthetic biology and precision molecular medicine.

Author Contributions: Y.Y.: conceptualization, draft preparation; L.Z.: draft preparation; F.Y.: conceptualization, supervision, draft preparation, writing—reviewing and editing. All authors have read and agreed to the published version of the manuscript.

Funding: This work was supported by the National Natural Science Foundation of China (grant 32471259).

Institutional Review Board Statement: Not applicable.

Informed Consent Statement: Not applicable.

Data Availability Statement: Not applicable.

Conflicts of Interest: The authors declare no conflict of interest.

Use of AI and AI-assisted technologies: During the preparation of this manuscript, the authors used Google Gemini to polish the language and improve the readability of Sections 1 and 5. After using this tool, the authors carefully reviewed and edited the content as needed, and take full responsibility for the final content of the published article.

References

1. Li, Z.; Deutscher, M.P. RNase E Plays an Essential Role in the Maturation of Escherichia Coli tRNA Precursors. *RNA* **2002**, *8*, 97–109. https://doi.org/10.1017/s1355838202014929.
2. Li, Z.; Pandit, S.; Deutscher, M.P. RNase G (CafA Protein) and RNase E Are Both Required for the 5′ Maturation of 16S Ribosomal RNA. *EMBO J.* **1999**, *18*, 2878–2885. https://doi.org/10.1093/emboj/18.10.2878.
3. Frank, D.N.; Pace, N.R. Ribonuclease P: Unity and Diversity in a tRNA Processing Ribozyme. *Annu. Rev. Biochem.* **1998**, *67*, 153–180. https://doi.org/10.1146/annurev.biochem.67.1.153.
4. Bisbal, C.; Silverman, R.H. Diverse Functions of RNase L and Implications in Pathology. *Biochimie* **2007**, *89*, 789–798. https://doi.org/10.1016/j.biochi.2007.02.006.
5. Chen, C.; Deutscher, M.P. Elevation of RNase R in Response to Multiple Stress Conditions. *J. Biol. Chem.* **2005**, *280*, 34393–34396. https://doi.org/10.1074/jbc.C500333200.
6. Rosenberg, H.F. RNase A Ribonucleases and Host Defense: An Evolving Story. *J. Leukoc. Biol.* **2008**, *83*, 1079–1087. https://doi.org/10.1189/jlb.1107725.
7. Thompson, J.E.; Kutateladze, T.G.; Schuster, M.C.; Venegas, F.D.; Messmore, J.M.; Raines, R.T. Limits to Catalysis by Ribonuclease A. *Bioorg. Chem.* **1995**, *23*, 471–481.
8. Sun, D.; Han, C.; Sheng, J. The Role of Human Ribonuclease A Family in Health and Diseases: A Systematic Review. *iScience* **2022**, *25*, 105284. https://doi.org/10.1016/j.isci.2022.105284.
9. Crow, Y.J.; Leitch, A.; Hayward, B.E.; Garner, A.; Parmar, R.; Griffith, E.; Ali, M.; Semple, C.; Aicardi, J.; Babul-hirji, R.; et al. Mutations in Genes Encoding Ribonuclease H2 Subunits Cause Aicardi-Goutieres Syndrome and Mimic Congenital Viral Brain Infection. *Nat. Genet.* **2006**, *38*, 910–916. https://doi.org/10.1038/ng1842.
10. Arraiano, C.M.; Andrade, J.M.; Domingues, S.; Guinote, I.B.; Malecki, M.; Matos, R.G.; Moreira, R.N.; Pobre, V.; Reis, F.P.; Saramago, M.; et al. The Critical Role of RNA Processing and Degradation in the Control of Gene Expression. *FEMS Microbiol. Rev.* **2010**, *34*, 883–923. https://doi.org/10.1111/j.1574-6976.2010.00242.x.
11. Garneau, N.L.; Wilusz, J.; Wilusz, C.J. The Highways and Byways of mRNA Decay. *Nat. Rev. Mol. Cell Biol.* **2007**, *8*, 113–126. https://doi.org/10.1038/nrm2104.
12. Parker, R.; Song, H. The Enzymes and Control of Eukaryotic mRNA Turnover. *Nat. Struct. Mol. Biol.* **2004**, *11*, 121–127. https://doi.org/10.1038/nsmb724.
13. Chakrabarti, A.; Jha, B.K.; Silverman, R.H. New Insights into the Role of RNase L in Innate Immunity. *J. Interf. Cytokine Res.* **2011**, *31*, 49–57. https://doi.org/10.1089/jir.2010.0120.
14. Boix, E.; Acquati, F.; Leonidas, D.; Pulido, D. Editorial: Role of Ribonucleases in Immune Response Regulation During Infection and Cancer. *Front. Immunol.* **2020**, *11*, 236. https://doi.org/10.3389/fimmu.2020.00236.
15. Nunes, I.V.; Breitenbach, L.; Pawusch, S.; Eigenbrod, T.; Ananth, S.; Schad, P.; Fackler, O.T.; Butter, F.; Dalpke, A.H.; Chen, L.S. Bacterial RNA Sensing by TLR8 Requires RNase 6 Processing and Is Inhibited by RNA 2′O-Methylation. *EMBO Rep.* **2024**, *25*, 4674–4692. https://doi.org/10.1038/s44319-024-00281-9.
16. Abudayyeh, O.O.; Gootenberg, J.S.; Konermann, S.; Joung, J.; Slaymaker, I.M.; Cox, D.B.T.; Shmakov, S.; Makarova, K.S.; Semenova, E.; Minakhin, L.; et al. C2c2 Is a Single-Component Programmable RNA-Guided RNA-Targeting CRISPR Effector. *Science* **2016**, *353*, aaf5573. https://doi.org/10.1126/science.aaf5573.
17. Kellner, M.J.; Koob, J.G.; Gootenberg, J.S.; Abudayyeh, O.O.; Zhang, F. SHERLOCK: Nucleic Acid Detection with CRISPR Nucleases. *Nat. Protoc.* **2019**, *14*, 2986–3012. https://doi.org/10.1038/s41596-019-0210-2.
18. Costales, M.G.; Matsumoto, Y.; Velagapudi, S.P.; Disney, M.D. Small Molecule Targeted Recruitment of a Nuclease to RNA. *J. Am. Chem. Soc.* **2018**, *140*, 6741–6744. https://doi.org/10.1021/jacs.8b01233.
19. Song, Y.; Cui, J.; Zhu, J.; Kim, B.; Kuo, M.L.; Potts, P.R. RNATACs: Multispecific Small Molecules Targeting RNA by Induced Proximity. *Cell Chem. Biol.* **2024**, *31*, 1101–1117. https://doi.org/10.1016/j.chembiol.2024.05.006.
20. Cuchillo, C.M.; Nogués, M.V.; Raines, R.T. Bovine Pancreatic Ribonuclease: Fifty Years of the First Enzymatic Reaction Mechanism. *Biochemistry* **2011**, *50*, 7835–7841. https://doi.org/10.1021/bi201075b.
21. Yoshida, H. The Ribonuclease T1 Family. *Methods Enzymol.* **2001**, *341*, 28–41. https://doi.org/10.1016/S0076-6879(01)41143-8.
22. Loverix, S.; Winqvist, A.; Strömberg, R.; Steyaert, J. Mechanism of RNase T1: Concerted Triester-like Phosphoryl Transfer via a Catalytic Three-Centered Hydrogen Bond. *Chem. Biol.* **2000**, *7*, 651–658. https://doi.org/10.1016/S1074-5521(00)00005-3.
23. Hyjek, M.; Figiel, M.; Nowotny, M. RNases H: Structure and Mechanism. *DNA Repair* **2019**, *84*, 102672. https://doi.org/10.1016/j.dnarep.2019.102672.
24. MacRae, I.J.; Doudna, J.A. Ribonuclease Revisited: Structural Insights into Ribonuclease III Family Enzymes. *Curr. Opin. Struct. Biol.* **2007**, *17*, 138–145. https://doi.org/10.1016/j.sbi.2006.12.002.
25. Nicholson, A.W. Ribonuclease III Mechanisms of Double-Stranded RNA Cleavage. *Wiley Interdiscip. Rev. RNA* **2014**,

5, 31–48. https://doi.org/10.1002/wrna.1195.
26. Howard, M.J.; Lim, W.H.; Fierke, C.A.; Koutmos, M. Mitochondrial Ribonuclease P Structure Provides Insight into the Evolution of Catalytic Strategies for Precursor-tRNA 5′ Processing. *Proc. Natl. Acad. Sci. USA* **2012**, *109*, 16149–16154. https://doi.org/10.1073/pnas.1209062109.
27. Nowotny, M.; Gaidamakov, S.A.; Crouch, R.J.; Yang, W. Crystal Structures of RNase H Bound to an RNA/DNA Hybrid: Substrate Specificity and Metal-Dependent Catalysis. *Cell* **2005**, *121*, 1005–1016. https://doi.org/10.1016/j.cell.2005.04.024.
28. Steitz, T.A.; Steitz, J.A. A General Two-Metal-Ion Mechanism for Catalytic RNA. *Proc. Natl. Acad. Sci. USA* **1993**, *90*, 6498–6502. https://doi.org/10.1073/pnas.90.14.6498.
29. Warshel, A.; Sharma, P.K.; Kato, M.; Xiang, Y.; Liu, H.; Olsson, M.H.M. Electrostatic Basis for Enzyme Catalysis. *Chem. Rev.* **2006**, *106*, 3210–3235. https://doi.org/10.1021/cr0503106.
30. Fried, S.D.; Boxer, S.G. Electric Fields and Enzyme Catalysis. *Annu. Rev. Biochem.* **2017**, *86*, 387–415. https://doi.org/10.1146/annurev-biochem-061516-044432.
31. Ruiz-Pernía, J.J.; Świderek, K.; Bertran, J.; Moliner, V.; Tuñón, I. Electrostatics as a Guiding Principle in Understanding and Designing Enzymes. *J. Chem. Theory Comput.* **2024**, *20*, 1783–1795. https://doi.org/10.1021/acs.jctc.3c01395.
32. Eberhart, M.E.; Wilson, T.R.; Johnston, N.W.; Alexandrova, A.N. Geometry of Charge Density as a Reporter on the Role of the Protein Scaffold in Enzymatic Catalysis: Electrostatic Preorganization and Beyond. *J. Chem. Theory Comput.* **2023**, *19*, 694–704. https://doi.org/10.1021/acs.jctc.2c01060.
33. Kamerlin, S.C.L.; Warshel, A. At the Dawn of the 21st Century: Is Dynamics the Missing Link for Understanding Enzyme Catalysis. *Proteins Struct. Funct. Bioinforma.* **2010**, *78*, 1339–1375. https://doi.org/10.1002/prot.22654.
34. Fried, S.D.; Bagchi, S.; Boxer, S.G. Measuring Electrostatic Fields in Both Hydrogen-Bonding and Non-Hydrogen-Bonding Environments Using Carbonyl Vibrational Probes. *J. Am. Chem. Soc.* **2013**, *135*, 11181–11192. https://doi.org/10.1021/ja403917z.
35. Kellerman, D.L.; York, D.M.; Piccirilli, J.A.; Harris, M.E. Altered (Transition) States: Mechanisms of Solution and Enzyme Catalyzed RNA 2′-O-Transphosphorylation. *Curr. Opin. Chem. Biol.* **2014**, *21*, 96–102. https://doi.org/10.1016/j.cbpa.2014.06.010.
36. Thompson, J.E.; Raines, R.T. Value of General Acid-Base Catalysis to Ribonuclease A. *J. Am. Chem. Soc.* **1994**, *116*, 5467–5468.
37. Avey, H.P.; Boles, M.O.; Carlisle, C.H.; Evans, S.A.; Morris, S.J.; Palmer, R.A.; Woolhouse, B.A.; Shall, S. Structure of Ribonuclease. *Nature* **1967**, *213*, 557–562. https://doi.org/10.1038/213557a0.
38. Gu, H.; Zhang, S.; Wong, K.Y.; Radak, B.K.; Dissanayake, T.; Kellerman, D.L.; Dai, Q.; Miyagi, M.; Anderson, V.E.; York, D.M.; et al. Experimental and Computational Analysis of the Transition State for Ribonuclease A-Catalyzed RNA 2′-O-Transphosphorylation. *Proc. Natl. Acad. Sci. USA* **2013**, *110*, 13002–13007. https://doi.org/10.1073/pnas.1215086110.
39. Fisher, B.M.; Ha, J.; Raines, R.T. Coulombic Forces in Protein-RNA Interactions: Binding and Cleavage by Ribonuclease A and Variants at Lys7, Arg10, and Lys66. *Biochemistry* **1998**, *37*, 12121–12132.
40. Fedor, M.J.; Williamson, J.R. The Catalytic Diversity of RNAs. *Nat. Rev. Mol. Cell Biol.* **2005**, *6*, 399–412. https://doi.org/10.1038/nrm1647.
41. Messmore, J.M.; Raines, R.T. Pentavalent Organo-Vanadates as Transition State Analogues for Phosphoryl Transfer Reactions. *J. Am. Chem. Soc.* **2000**, *122*, 9911–9916. https://doi.org/10.1021/ja0021058.
42. Raines, R.T. Ribonuclease A. *Chem. Rev.* **1998**, *98*, 1045–1065.
43. Arni, R.K.; Watanabe, L.; Ward, R.J.; Kreitman, R.J.; Kumar, K.; Walz, F.G. Three-Dimensional Structure of Ribonuclease T1 Complexed with an Isosteric Phosphonate Substrate Analogue of GpU: Alternate Substrate Binding Modes and Catalysis. *Biochemistry* **1999**, *38*, 2452–2461. https://doi.org/10.1021/bi982612q.
44. Ahsan, M.; Pindi, C.; Palermo, G. Emerging Mechanisms of Metal-Catalyzed RNA and DNA Modifications. *Annu. Rev. Phys. Chem.* **2025**, *76*, 497–518. https://doi.org/10.1146/annurev-physchem-082423-030241.
45. Palermo, G.; Cavalli, A.; Klein, M.L.; Alfonso-Prieto, M.; Dal Peraro, M.; De Vivo, M. Catalytic Metal Ions and Enzymatic Processing of DNA and RNA. *Acc. Chem. Res.* **2015**, *48*, 220–228. https://doi.org/10.1021/ar500314j.
46. Rosta, E.; Yang, W.; Hummer, G. Calcium Inhibition of Ribonuclease H1 Two-Metal Ion Catalysis. *J. Am. Chem. Soc.* **2014**, *136*, 3137–3144. https://doi.org/10.1021/ja411408x.
47. Zhao, Y.; Lu, M.; Zhang, H.; Hu, J.; Zhou, C.; Xu, Q.; Ul Hussain Shah, A.M.; Xu, H.; Wang, L.; Hua, Y. Structural Insights into Catalysis and Dimerization Enhanced Exonuclease Activity of RNase J. *Nucleic Acids Res.* **2015**, *43*, 5550–5559. https://doi.org/10.1093/nar/gkv444.
48. Sun, W.; Pertzev, A.; Nicholson, A.W. Catalytic Mechanism of Escherichia Coli Ribonuclease III: Kinetic and Inhibitor Evidence for the Involvement of Two Magnesium Ions in RNA Phosphodiester Hydrolysis. *Nucleic Acids Res.* **2005**, *33*, 807–815. https://doi.org/10.1093/nar/gki197.
49. Sun, W.; Li, G.; Nicholson, A.W. Mutational Analysis of the Nuclease Domain of Escherichia Coli Ribonuclease III. Identification of Conserved Acidic Residues That Are Important for Catalytic Function in Vitro. *Biochemistry* **2004**, *43*,

13054–13062. https://doi.org/10.1021/bi049258i.

50. De Vivo, M.; Dal Peraro, M.; Klein, M.L. Phosphodiester Cleavage in Ribonuclease H Occurs via an Associative Two-Metal-Aided Catalytic Mechanism. *J. Am. Chem. Soc.* **2008**, *130*, 10955–10962. https://doi.org/10.1021/ja8005786.
51. Rosta, E.; Nowotny, M.; Yang, W.; Hummer, G. Catalytic Mechanism of RNA Backbone Cleavage by Ribonuclease H from Quantum Mechanics / Molecular Mechanics Simulations. *J. Am. Chem. Soc.* **2011**, *133*, 8934–8941. https://doi.org/10.1021/ja200173a.
52. Steitz, T.A. A Mechanism for All Polymerases. *Nature* **1998**, *391*, 231–232.
53. Borišek, J.; Aupič, J.; Magistrato, A. Third Metal Ion Dictates the Catalytic Activity of the Two-Metal-Ion Pre-Ribosomal RNA-Processing Machinery. *Angew. Chemie Int. Ed.* **2024**, *63*, e202405819. https://doi.org/10.1002/anie.202405819.
54. Samara, N.L.; Yang, W. Cation Trafficking Propels RNA Hydrolysis. *Nat. Struct. Mol. Biol.* **2018**, *25*, 715–721. https://doi.org/10.1038/s41594-018-0099-4.
55. Griffin, M.A.; Davis, J.H.; Strobel, S.A. Bacterial Toxin RelE: A Highly Efficient Ribonuclease with Exquisite Substrate Specificity Using Atypical Catalytic Residues. *Biochemistry* **2013**, *52*, 8633–8642. https://doi.org/10.1021/bi401325c.
56. Neubauer, C.; Gao, Y.G.; Andersen, K.R.; Dunham, C.M.; Kelley, A.C.; Hentschel, J.; Gerdes, K.; Ramakrishnan, V.; Brodersen, D.E. The Structural Basis for mRNA Recognition and Cleavage by the Ribosome-Dependent Endonuclease RelE. *Cell* **2009**, *139*, 1084–1095. https://doi.org/10.1016/j.cell.2009.11.015.
57. Dunican, B.F.; Hiller, D.A.; Strobel, S.A. Transition State Charge Stabilization and Acid-Base Catalysis of mRNA Cleavage by the Endoribonuclease RelE. *Biochemistry* **2015**, *54*, 7048–7057. https://doi.org/10.1021/acs.biochem.5b00866.
58. Hiller, D.A.; Dunican, B.F.; Nallur, S.; Li, N.S.; Piccirilli, J.A.; Strobel, S.A. The Positively Charged Active Site of the Bacterial Toxin RelE Causes a Large Shift in the General Base PKa. *Biochemistry* **2020**, *59*, 1665–1671. https://doi.org/10.1021/acs.biochem.9b01047.
59. Haruki, M.; Tsunaka, Y.; Morikawa, M.; Iwai, S.; Kanaya, S. Catalysis by Escherichia Coli Ribonuclease HI Is Facilitated by a Phosphate Group of the Substrate. *Biochemistry* **2000**, *39*, 13939–13944.
60. Abdur, R.; Gerlits, O.O.; Gan, J.; Jiang, J.; Salon, J.; Kovalevsky, A.Y.; Chumanevich, A.A.; Weber, I.T.; Huang, Z. Novel Complex MAD Phasing and RNase H Structural Insights Using Selenium Oligonucleotides. *Acta Crystallogr. Sect. D Biol. Crystallogr.* **2014**, *70*, 354–361. https://doi.org/10.1107/S1399004713027922.
61. Domachowske, J.B.; Dyer, K.D.; Adams, A.G.; Leto, T.L.; Rosenberg, H.F. Eosinophil Cationic Protein/RNase 3 Is Another RNase A-Family Ribonuclease with Direct Antiviral Activity. *Nucleic Acids Res.* **1998**, *26*, 3358–3363. https://doi.org/10.1093/nar/26.14.3358.
62. Mallorquí-Fernández, G.; Pous, J.; Peracaula, R.; Aymamí, J.; Maeda, T.; Tada, H.; Yamada, H.; Seno, M.; De Llorens, R.; Gomis-Rüth, F.X.; et al. Three-Dimensional Crystal Structure of Human Eosinophil Cationic Protein (RNase 3) at 1.75 Å Resolution. *J. Mol. Biol.* **2000**, *300*, 1297–1307. https://doi.org/10.1006/jmbi.2000.3939.
63. Zhang, J.; Dyer, K.D.; Rosenberg, H.F. Human RNase 7: A New Cationic Ribonuclease of the RNase A Superfamily. *Nucleic Acids Res.* **2003**, *31*, 602–607. https://doi.org/10.1093/nar/gkg157.
64. Wang, H.; Schwaderer, A.L.; Kline, J.; Spencer, J.D.; Kline, D.; Hainsa, D.S. Contribution of Structural Domains to the Activity of Ribonuclease 7 against Uropathogenic Bacteria. *Antimicrob. Agents Chemother.* **2013**, *57*, 766–774. https://doi.org/10.1128/AAC.01378-12.
65. Huang, Y.C.; Lin, Y.M.; Chang, T.W.; Wu, S.J.; Lee, Y.S.; Chang, M.D.T.; Chen, C.; Wu, S.H.; Liao, Y. Di. The Flexible and Clustered Lysine Residues of Human Ribonuclease 7 Are Critical for Membrane Permeability and Antimicrobial Activity. *J. Biol. Chem.* **2007**, *282*, 4626–4633. https://doi.org/10.1074/jbc.M607321200.
66. Liang, Y.H.; Lavoie, M.; Comeau, M.A.; Elela, S.A.; Ji, X. Structure of a Eukaryotic RNase III Postcleavage Complex Reveals a Double-Ruler Mechanism for Substrate Selection. *Mol. Cell* **2014**, *54*, 431–444. https://doi.org/10.1016/j.molcel.2014.03.006.
67. MacRae, I.J.; Zhou, K.; Li, F.; Repic, A.; Brooks, A.N.; Cande, W.Z.; Adams, P.D.; Doudna, J.A. Structural Basis for Double-Stranded RNA Processing by Dicer. *Science* **2006**, *311*, 195–198. https://doi.org/10.1126/science.1121638.
68. Kwon, S.C.; Nguyen, T.A.; Choi, Y.-G.; Jo, M.H.; Hohng, S.; Kim, V.N.; Woo, J.-S. Structure of Human DROSHA. *Cell* **2016**, *164*, 81–90. https://doi.org/10.1016/j.cell.2015.12.019.
69. Partin, A.C.; Zhang, K.; Jeong, B.C.; Herrell, E.; Li, S.; Chiu, W.; Nam, Y. Cryo-EM Structures of Human Drosha and DGCR8 in Complex with Primary microRNA. *Mol. Cell* **2020**, *78*, 411-422.e4. https://doi.org/10.1016/j.molcel.2020.02.016.
70. Callaghan, A.J.; Marcaida, M.J.; Stead, J.A.; McDowall, K.J.; Scott, W.G.; Luisi, B.F. Structure of Escherichia Coli RNase E Catalytic Domain and Implications for RNA Turnover. *Nature* **2005**, *437*, 1187–1191. https://doi.org/10.1038/nature04084.
71. Jinek, M.; Coyle, S.M.; Doudna, J.A. Coupled 5′ Nucleotide Recognition and Processivity in Xrn1-Mediated mRNA Decay. *Mol. Cell* **2011**, *41*, 600–608. https://doi.org/10.1016/j.molcel.2011.02.004.
72. Stevens, A.; Poole, T.L. 5′-Exonuclease-2 of Saccharomyces Cerevisiae. *J. Biol. Chem.* **1995**, *270*, 16063–16069. https://doi.org/10.1074/jbc.270.27.16063.
73. Stevens, A. 5′-Exoribonuclease 1: Xrn 1. *Methods Enzymol.* **2001**, *342*, 251–259. https://doi.org/10.1016/S0076-6879(01)42549-3.

74. Chamberlain, A.R.; Huynh, L.; Huang, W.; Taylor, D.J.; Harris, M.E. The Specificity Landscape of Bacterial Ribonuclease P. *J. Biol. Chem.* **2024**, *300*, 105498. https://doi.org/10.1016/j.jbc.2023.105498.
75. Lan, P.; Tan, M.; Zhang, Y.; Niu, S.; Chen, J.; Shi, S.; Qiu, S.; Wang, X.; Peng, X.; Cai, G.; et al. Structural Insight into Precursor tRNA Processing by Yeast Ribonuclease P. *Science*, **2018**, *362*, eaat6678. https://doi.org/10.1126/science.aat6678.
76. Wang, P.; Lin, J.; Zheng, X.; Xu, X. RNase P: Beyond Precursor tRNA Processing. *Genom. Proteom. Bioinforma.* **2024**, *22*, qzae016. https://doi.org/10.1093/gpbjnl/qzae016.
77. Tambe, A.; East-Seletsky, A.; Knott, G.J.; Doudna, J.A.; O'Connell, M.R. RNA Binding and HEPN-Nuclease Activation Are Decoupled in CRISPR-Cas13a. *Cell Rep.* **2018**, *24*, 1025–1036. https://doi.org/10.1016/j.celrep.2018.06.105.
78. Yan, W.X.; Hunnewell, P.; Alfonse, L.E.; Carte, J.M.; Keston-Smith, E.; Sothiselvam, S.; Garrity, A.J.; Chong, S.; Makarova, K.S.; Koonin, E.V.; et al. Functionally Diverse Type V CRISPR-Cas Systems. *Science* **2019**, *363*, 88–91. https://doi.org/10.1126/science.aav7271.
79. Charlesworth, C.T.; Deshpande, P.S.; Dever, D.P.; Camarena, J.; Lemgart, V.T.; Cromer, M.K.; Vakulskas, C.A.; Collingwood, M.A.; Zhang, L.; Bode, N.M.; et al. Identification of Preexisting Adaptive Immunity to Cas9 Proteins in Humans. *Nat. Med.* **2019**, *25*, 249–254. https://doi.org/10.1038/s41591-018-0326-x.
80. Wagner, D.L.; Amini, L.; Wendering, D.J.; Burkhardt, L.M.; Akyüz, L.; Reinke, P.; Volk, H.D.; Schmueck-Henneresse, M. High Prevalence of Streptococcus Pyogenes Cas9-Reactive T Cells within the Adult Human Population. *Nat. Med.* **2019**, *25*, 242–248. https://doi.org/10.1038/s41591-018-0204-6.
81. Mehta, A.; Merkel, O.M. Immunogenicity of Cas9 Protein. *J. Pharm. Sci.* **2020**, *109*, 62–67. https://doi.org/10.1016/j.xphs.2019.10.003.
82. Ruseska, I.; Zimmer, A. Internalization Mechanisms of Cell-Penetrating Peptides. *Beilstein J. Nanotechnol.* **2020**, *11*, 101–123. https://doi.org/10.3762/bjnano.11.10.
83. Perr, J.; Langen, A.; Almahayni, K.; Mo, L.; Zaro, B.W.; Flynn, R.A. RNA-Binding Proteins and GlycoRNAs Form Domains on the Cell Surface for Cell-Penetrating Peptide Entry. *Cell* **2025**, *188*, 1878-1895.e25. https://doi.org/10.1016/j.cell.2025.01.040.